Applied Mathematics Letters 163 (2025) 109439

Contents lists available at ScienceDirect

Applied Mathematics Letters

journal homepage: www.elsevier.com/locate/aml

Regular article

A second-order accurate numerical method with unconditional energy stability for the Lifshitz–Petrich equation on curved surfaces

Xiaochuan Hu [a], Qing Xia [a], Binhu Xia [b], Yibao Li [a,*]

[a] School of Mathematics and Statistics, Xi'an Jiaotong University, Xi'an 710049, China
[b] School of Computer Science, Xijing University, Xi'an 710123, China

ARTICLE INFO

Keywords:
Second-order algorithm
Unconditional stability
Lifshitz–Petrich crystal model
Curved surfaces

ABSTRACT

In this paper, we introduce an efficient numerical algorithm for solving the Lifshitz–Petrich equation on closed surfaces. The algorithm involves discretizing the surface with a triangular mesh, allowing for an explicit definition of the Laplace–Beltrami operator based on the neighborhood information of the mesh elements. To achieve second-order temporal accuracy, the backward differentiation formula scheme and the scalar auxiliary variable method are employed for Lifshitz–Petrich equation. The discrete system is subsequently solved using the biconjugate gradient stabilized method, with incomplete LU decomposition of the coefficient matrix serving as a preprocessor. The proposed algorithm is characterized by its simplicity in implementation and second-order precision in both spatial and temporal domains. Numerical experiments are conducted to validate the unconditional energy stability and efficacy of the algorithm.

1. Introduction

Crystals are essential in many processes that occur in nature as well as in industry [1,2]. There is a growing concentration of interest on the processes of growth [3,4] and transition [5] of varied crystalline formations, in addition to their interface dynamics [6]. Many numerical methods have been studied for crystal models, such as convex splitting method [7], multigrid method [8,9] and adaptive time step method [10], method without artificial curvature effect [11]. Shechtmann and Blech [12] discovered quasicrystals in a rapidly cooled aluminum-manganese alloy. The unique properties of crystals and quasicrystals have a broad spectrum of applications, such as thermal insulation [13], optical materials [14] and additive manufacturing [15]. Therefore, research on the formation of micro-patterns is crucial for forecasting material characteristics and lowering experimental expenses [16,17]. The energy proposed by the Lifshitz–Petrich (LP) model has the following form:

$$\mathcal{E}(\phi) = \int_{\Omega} \frac{\phi}{2} L_1^2(L_2^2 + \xi^2)\phi + F(\phi)\mathrm{d}\mathbf{x}, \tag{1}$$

where $L_1 = \Delta + I$, $L_2 = \Delta + \eta^2 I$, I is the identity operator. $F(\phi) = \frac{\phi^4}{4} - \frac{\alpha\phi^3}{3} - \frac{\epsilon\phi^2}{2}$, and $\xi, \eta, \alpha, \epsilon$ are physical parameters. Utilizing the variational method on Eq. (1) yields the expression for chemical potential: $\frac{\delta\mathcal{E}(\phi)}{\delta\phi} = L_1^2(L_2^2 + \xi^2)\phi + F'(\phi)$. Employing the L^2-gradient flow, the principal governing equation is formulated as follows:

$$\frac{\partial\phi}{\partial t} = -\frac{\delta\mathcal{E}(\phi)}{\delta\phi} = -L_1^2(L_2^2 + \xi^2)\phi - F'(\phi) = -(\Delta + 1)^2\Big((\Delta + \eta^2)^2 + \xi^2\Big)\phi - F'(\phi). \tag{2}$$

* Corresponding author.
E-mail address: yibaoli@xjtu.edu.cn (Y. Li).

https://doi.org/10.1016/j.aml.2024.109439
Received 15 October 2024; Received in revised form 17 December 2024; Accepted 17 December 2024
Available online 24 December 2024
0893-9659/© 2024 Elsevier Ltd. All rights are reserved, including those for text and data mining, AI training, and similar technologies.

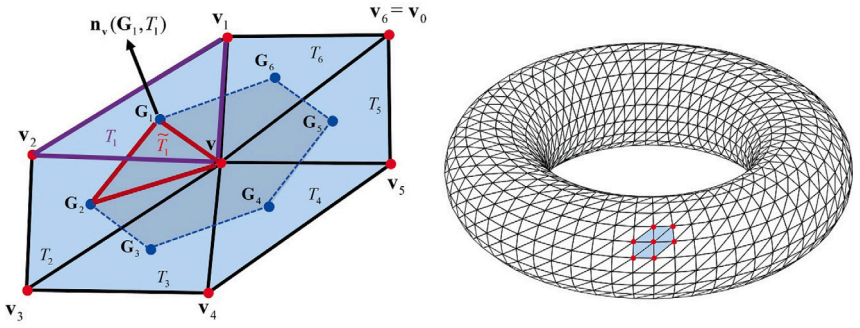

Fig. 1. The right: a closed surface triangular mesh; The left: a grid vertex with the adjacent vertices.

In the case of flat surfaces, many related numerical algorithms have been studied, such as finite difference method [18,19], finite element method [20,21], Galerkin method [22], Fourier spectrum method [23,24], operator splitting method [25,26], threshold dynamics method [27], adaptive refinement mesh method [28], data assimilation method [29,30]. For curved surfaces, Kim et al. [31] introduced an efficient numerical approach for solving the conservative Allen–Cahn equation on various surfaces, incorporating a space–time-dependent Lagrange multiplier to ensure the conservation of the total quantity. Li et al. [32] proposed a computational framework for the multi-component Cahn–Hilliard system on surfaces, which is proved to be unconditional energy stability and mass conservation. Xia et al. [33] proposed an efficient surface computational system for solving thermal fluids problems, which exhibited second-order spatial and temporal accuracy. Yang et al. [34] proposed a practical numerical method for solving the two-component phase-field crystal model on curved surfaces, which incorporated a vacancy effect. Xia et al. [35] proposed a framework for calculating the Swift–Hohenberg equation over arbitrarily curved surfaces, which has second-order temporal accuracy and is unconditionally energy stable. However, for the LP equation depicting various crystal or quasicrystal types, there are few research studies on curved surfaces. It is necessary to modify the numerical algorithm for LP equation on curved surfaces.

This paper aims to construct a discretization method for the LP equation to model crystal or quasicrystal formation on closed surfaces. The equation, derived from the LP energy model via variational principles, employs the backward differentiation formula scheme (BDF) and the scalar auxiliary variable method (SAV) [36,37] for temporal discretization, ensuring second-order accuracy and unconditional energy stability. For spatial discretization, we employ triangular elements to mesh the closed surface and derive a discrete Laplace–Beltrami operator, ensuring second-order spatial accuracy. The biconjugate gradient stabilized method enhances efficiency for solving sparse linear systems. Numerical tests validate the method's correctness in simulating crystal or quasicrystal formation.

The structure of this paper is arranged as follows. In Section 2, we derive the second-order numerical scheme of the LP equation on a surface, and then prove its unconditional energy stability. In Section 3, we demonstrate the correctness of the algorithm through numerical experiments. In Section 4, we give the conclusion.

2. Numerical scheme

2.1. Discreted Laplace–Beltrami operators on curved surfaces

For any regular closed surface S, it can be discretized by triangular elements. We can define $F := \{T_i | 1 \le i \le N_T\}$ as the set of all triangles and $V := \{\mathbf{v}_i | 1 \le i \le N_v\}$ as the set of all vertices. Fig. 1 illustrates that for any given vertex $\mathbf{v} \in V$, there are p vertices surrounding it. These vertices are sequentially labeled in a counterclockwise direction, with the vertex $\mathbf{v}_j$ being one of them, $\mathbf{v}_0 = \mathbf{v}_p$. Let $\mathbf{G}_j := \frac{\mathbf{v}+\mathbf{v}_j+\mathbf{v}_{j+1}}{3}$ be the centroid of a triangle T_j composed of vertices $\mathbf{v}$, $\mathbf{v}_j$, and $\mathbf{v}_{j+1}$. For any function ϕ on a surface, we can define $\nabla_h \phi(\mathbf{G}_j)$ as follows:

$$\nabla_h \phi(\mathbf{G}_j) := \alpha_j(\mathbf{v}_j - \mathbf{G}_j) + \beta_j(\mathbf{v}_{j+1} - \mathbf{G}_j), \tag{3}$$

where α_j and β_j meet the following conditions:

$$\begin{pmatrix} \langle \mathbf{v}_j - \mathbf{G}_j, \mathbf{v} - \mathbf{G}_j \rangle & \langle \mathbf{v}_{j+1} - \mathbf{G}_j, \mathbf{v} - \mathbf{G}_j \rangle & \|\mathbf{v} - \mathbf{G}_j\|^2 \\ \langle \mathbf{v}_j - \mathbf{G}_j, \mathbf{v}_j - \mathbf{G}_j \rangle & \langle \mathbf{v}_{j+1} - \mathbf{G}_j, \mathbf{v}_j - \mathbf{G}_j \rangle & \|\mathbf{v}_j - \mathbf{G}_j\|^2 \\ \langle \mathbf{v}_j - \mathbf{G}_j, \mathbf{v}_{j+1} - \mathbf{G}_j \rangle & \langle \mathbf{v}_{j+1} - \mathbf{G}_j, \mathbf{v}_{j+1} - \mathbf{G}_j \rangle & \|\mathbf{v}_{j+1} - \mathbf{G}_j\|^2 \end{pmatrix} \begin{pmatrix} \alpha_j \\ \beta_j \\ \gamma_j \end{pmatrix} = \begin{pmatrix} \phi(\mathbf{v}) - \phi(\mathbf{G}_j) \\ \phi(\mathbf{v}_j) - \phi(\mathbf{G}_j) \\ \phi(\mathbf{v}_{j+1}) - \phi(\mathbf{G}_j) \end{pmatrix}. \tag{4}$$

Using Green's formula and Eq. (4), Laplace–Beltrami operator can be approximated as:

$$\begin{aligned} \Delta_h \phi(\mathbf{v}) = \frac{1}{A(\mathbf{v})} \sum_{j=0}^{p-1} \frac{\|\mathbf{G}_{j+1} - \mathbf{G}_j\|}{6} \Big(& 2 \left\langle \nabla_h \phi(\mathbf{G}_j), \mathbf{n}_{\mathbf{v}}(\mathbf{G}_j, T_j) \right\rangle + 2 \left\langle \nabla_h \phi(\mathbf{G}_{j+1}), \mathbf{n}_{\mathbf{v}}(\mathbf{G}_{j+1}, T_j) \right\rangle \\ & + \left\langle \nabla_h \phi(\mathbf{G}_j), \mathbf{n}_{\mathbf{v}}(\mathbf{G}_{j+1}, T_j) \right\rangle + \left\langle \nabla_h \phi(\mathbf{G}_{j+1}), \mathbf{n}_{\mathbf{v}}(\mathbf{G}_j, T_j) \right\rangle \Big). \end{aligned} \tag{5}$$

The area at vertex $\mathbf{v}$ is defined as $A(\mathbf{v}) := \sum_{j=0}^{p-1} \left|\tilde{T}_j\right|$, where $\left|\tilde{T}_j\right|$ represents the area of a triangle $\tilde{T}_j$ consisting of three vertices $\mathbf{v}$, $\mathbf{G}_j$, and $\mathbf{G}_{j+1}$. The external normal vectors $\mathbf{n}_{\mathbf{v}}(\mathbf{G}_j, T_j)$ and $\mathbf{n}_{\mathbf{v}}(\mathbf{G}_{j+1}, T_j)$ are defined as follows:

$$\mathbf{n}_{\mathbf{v}}(\mathbf{G}_j, T_j) := \frac{(\mathbf{G}_{j+1} - \mathbf{G}_j) \times \mathbf{N}_j}{\|\mathbf{G}_{j+1} - \mathbf{G}_j) \times \mathbf{N}_j\|} \text{ and } \mathbf{n}_{\mathbf{v}}(\mathbf{G}_{j+1}, T_j) := \frac{(\mathbf{G}_{j+1} - \mathbf{G}_j) \times \mathbf{N}_{j+1}}{\|\mathbf{G}_{j+1} - \mathbf{G}_j) \times \mathbf{N}_{j+1}\|}, \tag{6}$$

where $\mathbf{N}_j$ denotes the unit normal vector corresponding to T_j.

2.2. Numerical method of LP equation on curved surfaces

In the framework, Eq. (2) can be equivalent to the following form:

$$\begin{cases} \phi_t = -L_1^2(L_2^2 + \xi^2)\phi - \dfrac{r(t)}{\sqrt{E_1(\phi) + C_0}} F'(\phi), \\ r_t = \dfrac{1}{2\sqrt{E_1(\phi) + C_0}} \displaystyle\int_\Omega F'(\phi)\phi_t \mathrm{d}\mathbf{x}, \end{cases} \tag{7}$$

Here, $-C_0$ is the lower bound of $E_1(\phi) := \int_\Omega F(\phi)\mathrm{d}\mathbf{x}$, $r(t) = \sqrt{E_1(\phi) + C_0}$ is the introduced scalar auxiliary variable. In this paper, we discretize LP equation using BDF and SAV scheme:

$$\begin{cases} \dfrac{3\phi^{n+1} - 4\phi^n + \phi^{n-1}}{2\Delta t} = -L_1^2(L_2^2 + \xi^2)\phi^{n+1} - \dfrac{r^{n+1}}{\sqrt{E_1(\tilde{\phi}^{n+1}) + C_0}} F'(\tilde{\phi}^{n+1}), \\ \dfrac{3r^{n+1} - 4r^n + r^{n-1}}{2\Delta t} = \Big(\dfrac{F'(\tilde{\phi}^{n+1})}{2\sqrt{E_1(\tilde{\phi}^{n+1}) + C_0}}, \dfrac{3\phi^{n+1} - 4\phi^n + \phi^{n-1}}{2\Delta t} \Big)_h, \end{cases} \tag{8}$$

where $\phi^{n+1}, \phi^n, \phi^{n-1}$ and $\tilde{\phi}^{n+1}$ are $N_v \times 1$ column vectors. $\tilde{\phi}^{n+1} = 2\phi^n - \phi^{n-1}$, $E_1(\tilde{\phi}^{n+1}) = (F(\tilde{\phi}^{n+1}), 1)_h$, the discrete inner product on a surface can be defined as $(\phi, \psi)_h := \sum_{i=1}^{N_v} \phi_i \psi_i A(\mathbf{v}_i)$. Further, we discretize Eq. (8) and we write it as the following matrix representation:

$$\begin{pmatrix} \frac{3}{2}\mathcal{I} + \Delta t \mathcal{P} & \frac{\Delta t F'(\tilde{\phi}^{n+1})}{\sqrt{E_1 + C_0}} \\ \frac{-3(A \circ F'(\tilde{\phi}^{n+1}))^{\mathrm{T}}}{2\sqrt{E_1 + C_0}} & 3 \end{pmatrix} \begin{pmatrix} \phi_1^{n+1} \\ \vdots \\ \phi_{N_v}^{n+1} \\ r^{n+1} \end{pmatrix} = \begin{pmatrix} 2\phi_1^n - \frac{\phi_1^{n-1}}{2} \\ \vdots \\ 2\phi_{N_v}^n - \frac{\phi_{N_v}^{n-1}}{2} \\ 4r^n - r^{n-1} + (\frac{F'(\tilde{\phi}^{n+1})}{2\sqrt{E_1 + C_0}}, -4\phi^n + \phi^{n-1})_h \end{pmatrix}. \tag{9}$$

Here, $\mathcal{I}$ is the $N_v \times N_v$ identity matrix. According to Eqs. (2) and (9), The matrix $\mathcal{P}$ corresponding to operator $L_1^2(L_2^2 + \xi^2)$ is defined as $\mathcal{P} := (\mathcal{L} + \mathcal{I})^2\big((\mathcal{L} + \eta^2\mathcal{I})^2 + \xi^2\mathcal{I}\big)$, where $\mathcal{L}$ is a $N_v \times N_v$ matrix obtained by (5) corresponding to the discrete Laplace–Beltrami operator on a surface mesh. A and $F'(\tilde{\phi}^{n+1})$ are $N_v \times 1$ column vectors with elements $A(\mathbf{v}_i)$ and $F'(\tilde{\phi}_i^{n+1}), i = 1, \ldots, N_v$, respectively. The operation $\mathbf{a} \circ \mathbf{b}$ represents Hadamard product of column vectors $\mathbf{a}$ and $\mathbf{b}$. In order to speed up the calculation, we adopt the biconjugate gradient stabilized method [38], and use the incomplete LU decomposition of the coefficient matrix as the preprocessor.

2.3. Discrete unconditional energy stability

Theorem. *The solution of Eq. (9) satisfy the energy dissipation property*

$$\mathcal{E}_d(\phi^{n+1}) - \mathcal{E}_d(\phi^n) \le 0, \tag{10}$$

where $\mathcal{E}_d(\phi^{n+1})$ is the discrete energy, which is defined as

$$\mathcal{E}_d(\phi^{n+1}) := \frac{1}{4\Delta t}(\|\phi^{n+1}\|_L^2 + \|2\phi^{n+1} - \phi^n\|_L^2) + \frac{1}{2\Delta t}((r^{n+1})^2 + (2r^{n+1} - r^n)^2). \tag{11}$$

Here, the discrete norm is defined as $\|\phi\|^2 := (\phi, \phi)_h, \|\phi\|_L^2 := (\phi, L_1^2(L_2^2 + \xi^2)\phi)_h$.

Proof. By introducing the intermediate variable v^{n+1}, Eq. (8) can be turned into the following discrete form:

$$\begin{cases} \dfrac{3\phi^{n+1} - 4\phi^n + \phi^{n-1}}{2\Delta t} = v^{n+1}, \\ v^{n+1} = -L_1^2(L_2^2 + \xi^2)\phi^{n+1} - \dfrac{r^{n+1}}{\sqrt{E_1 + C_0}} F'(\tilde{\phi}^{n+1}), \\ \dfrac{3r^{n+1} - 4r^n + r^{n-1}}{2\Delta t} = \Big(\dfrac{F'(\tilde{\phi}^{n+1})}{2\sqrt{E_1 + C_0}}, \dfrac{3\phi^{n+1} - 4\phi^n + \phi^{n-1}}{2\Delta t} \Big)_h. \end{cases} \tag{12}$$

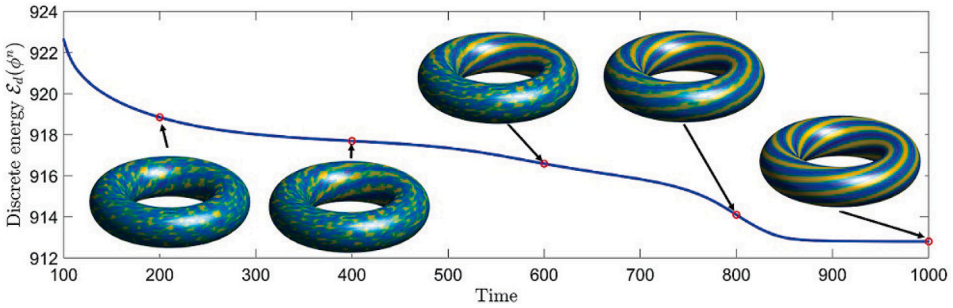

Fig. 2. Time evolution of non-increasing discrete energy.

By taking the discrete inner products of first two equations in Eq. (12) with v^{n+1} and $\frac{3\phi^{n+1}-4\phi^n+\phi^{n-1}}{2\Delta t}$ in turn, respectively, both sides of the third equation in Eq. (12) are multiplied by $2r^{n+1}$, the following formula can be obtained:

$$\Big(\frac{3\phi^{n+1}-4\phi^n+\phi^{n-1}}{2\Delta t}, v^{n+1}\Big)_h = \|v^{n+1}\|_h^2, \tag{13}$$

$$\Big(\frac{3\phi^{n+1}-4\phi^n+\phi^{n-1}}{2\Delta t}, v^{n+1}\Big)_h = \Big(-L_1^2(L_2^2+\xi^2)\phi^{n+1} - \frac{r^{n+1}}{\sqrt{E_1+C_0}}F'(\tilde{\phi}^{n+1}), \frac{3\phi^{n+1}-4\phi^n+\phi^{n-1}}{2\Delta t}\Big)_h, \tag{14}$$

$$2r^{n+1}\frac{3r^{n+1}-4r^n+r^{n-1}}{2\Delta t} = 2r^{n+1}\Big(\frac{F'(\tilde{\phi}^{n+1})}{2\sqrt{E_1+C_0}}, \frac{3\phi^{n+1}-4\phi^n+\phi^{n-1}}{2\Delta t}\Big)_h. \tag{15}$$

By substituting Eq. (15) into Eq. (14), we obtain:

$$\begin{aligned} -\|v^{n+1}\|_h^2 &= \Big(L_1^2(L_2^2+\xi^2)\phi^{n+1}, \frac{3\phi^{n+1}-4\phi^n+\phi^{n-1}}{2\Delta t}\Big)_h + 2r^{n+1}\frac{3r^{n+1}-4r^n+r^{n-1}}{2\Delta t} \\ &= \frac{1}{4\Delta t}(\|\phi^{n+1}\|_L^2 + \|2\phi^{n+1}-\phi^n\|_L^2 - \|\phi^n\|_L^2 - \|2\phi^n-\phi^{n-1}\|_L^2 + \|\phi^{n+1}-2\phi^n+\phi^{n-1}\|_L^2) \\ &+ \frac{1}{2\Delta t}((r^{n+1})^2 + (2r^{n+1}-r^n)^2 - (r^n)^2 - (2r^n-r^{n-1})^2 + (r^{n+1}-2r^n+r^{n-1})^2) \\ &= \mathcal{E}_d(\phi^{n+1}) - \mathcal{E}_d(\phi^n) + \frac{1}{4\Delta t}\|\phi^{n+1}-2\phi^n+\phi^{n-1}\|_L^2 + \frac{1}{2\Delta t}(r^{n+1}-2r^n+r^{n-1})^2. \end{aligned} \tag{16}$$

Eq. (16) implies that $\mathcal{E}_d(\phi^{n+1}) - \mathcal{E}_d(\phi^n) \le 0$.

3. Numerical experiments

3.1. Energy dissipation test

In this section, we verify the unconditional energy stability of the algorithm by numerical experiments. In this article, ξ and η are set to 0.01 and $2\cos(\frac{\pi}{12})$, respectively. The study is conducted on a torus with 4500 vertices, where adjacent vertex distances range from 1 to 2.4358. The initial conditions are set as $\phi(\mathbf{v},0) = -0.25 + 0.01\text{rand}(\mathbf{v})$, where rand($\mathbf{v}$) represents a random number ranging from -1 to 1. We set the parameters needed for the equation as $\Delta t = 0.1, \alpha = 0.077, \epsilon = 0.063, C_0 = 100$. Fig. 2 shows the energy evolution during crystallization on a torus, with $\phi(\mathbf{v},t)$ transitioning from a chaotic to a lamellar form.

3.2. Contrast test between curved and flat surfaces

In this section, we simulate the formation process of three kinds of crystals on the torus and the flat surface, respectively. Since periodic boundary conditions are used for the rectangular region of the flat surface, which is equivalent to the torus in $\mathbb{R}^3$, we use torus for numerical calculations. The 6-fold body centered cubic (BCC), transformed 6-fold crystalline state (T6), and Lamella state are studied in this section. For the simulation on curved surfaces, we adopt the BDF-SAV method proposed in this paper, and for the simulation on flat surfaces, the method proposed in [5] is adopted. To simulate the evolution process of different crystal types on the torus, different parameters (α, ϵ) need to be set respectively: BCC (0.6871,0.001), T6 (0.75,0.016), Lamella (0.005,0.016). In addition, the torus in this section has 60,000 vertices, the minimum and maximum distance between adjacent vertices are 1 and 1.8437, respectively, and the time steps taken are $\Delta t = 0.1$ and $C_0 = 400$. The initial conditions are established as $\phi(\mathbf{v},0) = \bar{\phi} + 0.01\text{rand}(\mathbf{v})$, for Lamella state, $\bar{\phi}$ is set to -0.25, while for BCC and T6, $\bar{\phi}$ is set to 0. Fig. 3 illustrates a pronounced local resemblance between the crystal on the torus and the flat surface. Moreover, it demonstrates the method's efficacy in mapping crystal evolution from a flat surface onto arbitrary closed surfaces.

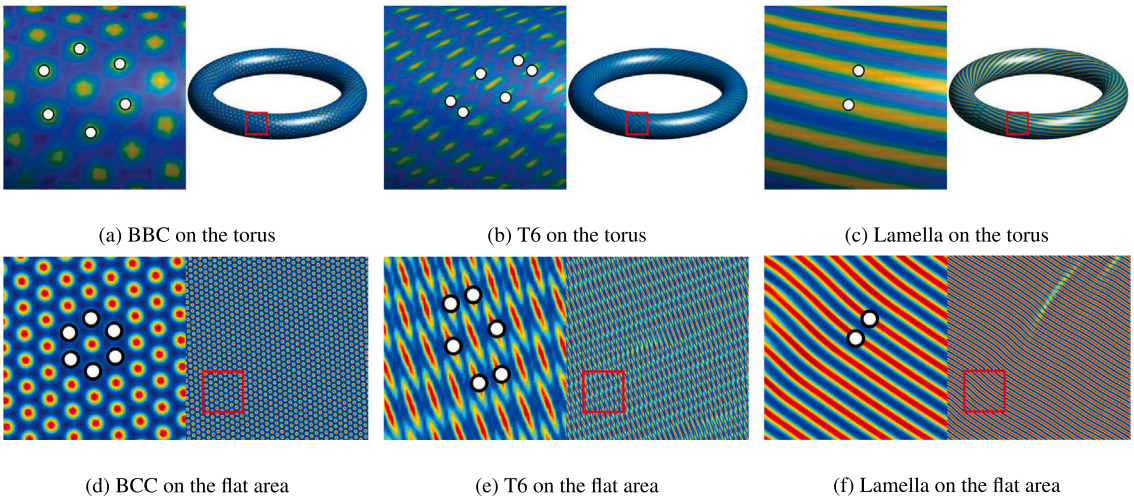

(a) BBC on the torus (b) T6 on the torus (c) Lamella on the torus

(d) BCC on the flat area (e) T6 on the flat area (f) Lamella on the flat area

Fig. 3. Crystal forms on the torus and flat surfaces. The left detail magnifies red-outlined area and crystals marked in white.

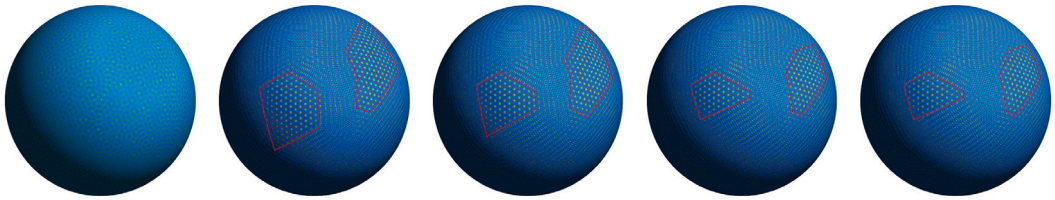

(a) $t = 1000$ (b) $t = 3000$ (c) $t = 5000$ (d) $t = 7000$ (e) $t = 9000$

Fig. 4. Crystal formation and boundary evolution on a sphere surface. The red line marks the boundary between the two crystals..

3.3. Grain boundaries change test on a curved surface

In this section, we conduct numerical tests on a sphere of radius 115.6134, utilizing a triangular mesh of 163,824 vertices, where the vertex spacing ranges from 1 to 1.1951. We take the time step $\Delta t = 0.1, \alpha = 1.007, \epsilon = 0.001$, $C_0 = 400$. The initial state is $\phi(\mathbf{v}, 0) = 0.01\text{rand}(\mathbf{v})$, Fig. 4 delineates the outcomes of the computational experiments, wherein the temporal progression is denoted below each illustration. It can be seen that with the passage of time, the pattern on the sphere gradually evolved from a chaotic state to a crystalline state. At $t = 3000$, the sphere exhibits two predominant crystalline states, identified as BCC and T6. The boundary between the phases is indicated by a red line, showing that the crystal state boundary evolves with increasing t before stabilizing.

3.4. Test of crystal formation on sharp surfaces

In this section, we perform a numerical test on a cube surface with a side length of 64, utilizing a triangular mesh of 24,578 vertices, where the vertex spacing ranges from 1 to 1.414. We set $\Delta t = 0.1, \alpha = 0.707, \epsilon = 0.005, C_0 = 400$. The initial state is $\phi(\mathbf{v}, 0) = 0.01\text{rand}(\mathbf{v})$, Fig. 5 shows the formation process of BCC type crystals on the surface of the cube. It can be seen that our algorithm performs better at sharp edges and corners, and the texture of BCC crystals is also clear near the edges and corners of the cube.

4. Conclusion

In this work, we developed an efficient numerical method aimed at solving LP equation on closed surfaces. The method involves using triangular mesh on a surface for discretization of differential operators. Our proposed algorithm is based on BDF and SAV, and exhibits second-order accuracy in both time and space dimensions. We conducted a series of simulation experiments to verify the algorithm's performance, including a discrete energy dissipation test, a comparison test between torus and flat surfaces, and a crystal interface evolution test. Results confirmed the proposed algorithm's unconditional energy stability, suitable for simulating surface crystallization.

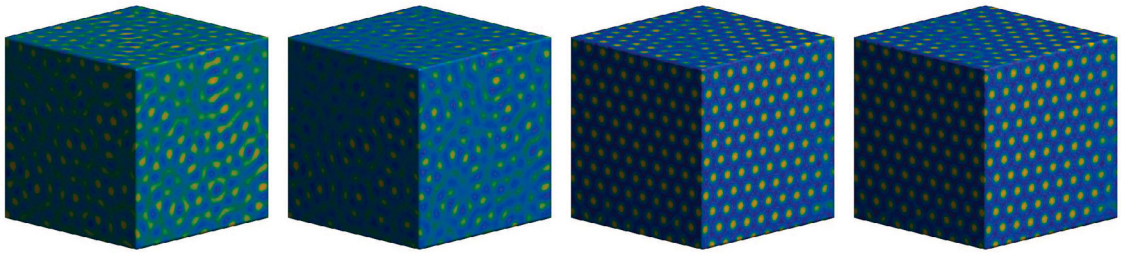

(a) $t = 400$ (b) $t = 800$ (c) $t = 1200$ (d) $t = 1600$

Fig. 5. Crystal formation process on the surface of the cube.

Acknowledgments

This work is supported by Natural Science Basic Research Program of Shaanxi (Program No. 2024JC-YBMS-016) and Shaanxi Fundamental Science Research Project for Mathematics and Physics (Grant No. 23JSQ054).

Data availability

No data was used for the research described in the article.

References

[1] D. Erdemir, A.Y. Lee, A.S. Myerson, Nucleation of crystals from solution: classical and two-step models, Acc. Chem. Res. 42 (5) (2009) 621–629.
[2] J. Kim, H.G. Lee, Unconditionally energy stable second-order numerical scheme for the Allen–Cahn equation with a high-order polynomial free energy, Adv. Difference Equ. 2021 (2021) 1–13.
[3] Y. Li, D.S. Lee, H.G. Lee, et al., A robust and accurate phase-field simulation of snow crystal growth, J. Korean Soc. Ind. Appl. Math. 16 (1) (2012) 15–29.
[4] Y. Li, K. Qin, Q. Xia, et al., A second-order unconditionally stable method for the anisotropic dendritic crystal growth model with an orientation-field, Appl. Numer. Math. 184 (2023) 512–526.
[5] Q. Xia, J. Yang, J. Kim, et al., On the phase field based model for the crystalline transition and nucleation within the Lagrange multiplier framework, J. Comput. Phys. (2024) 113158.
[6] D. Wang, B. Osting, X.P. Wang, Interface dynamics for an Allen–Cahn-type equation governing a matrix-valued field, Multisc. Model. Simul. 17 (4) (2019) 1252–1273.
[7] J. Yang, Unconditionally energy-stable linear convex splitting algorithm for the L2 quasicrystals, Comput. Phys. Comm. 295 (2024) 108984.
[8] Y. Li, J. Kim, Phase-field simulations of crystal growth with adaptive mesh refinement, Int. J. Heat Mass Transfer 55 (25–26) (2012) 7926–7932.
[9] Q. Xia, X. Jiang, Y. Li, A modified and efficient phase field model for the biological transport network, J. Comput. Phys. 488 (2023) 112192.
[10] Y. Li, J. Kim, An efficient and stable compact fourth-order finite difference scheme for the phase field crystal equation, Comput. Methods Appl. Mech. Engrg. 319 (2017) 194–216.
[11] Y. Li, Q. Yu, S. Ham, et al., A phase-field model without artificial curvature effect for the crystal growth simulation, Int. J. Heat Mass Transfer 203 (2023) 123847.
[12] D. Shechtman, I. Blech, D. Gratias, et al., Metallic phase with long-range orientational order and no translational symmetry, Phys. Rev. Lett. 53 (20) (1984) 1951.
[13] P. Archambault, C. Janot, Thermal conductivity of quasicrystals and associated processes, MRS Bull. 22 (11) (1997) 48–53.
[14] E.R. Brandão, C.H. Costa, M.S. Vasconcelos, et al., Octonacci photonic quasicrystals, Opt. Mater. 46 (2015) 378–383.
[15] Q. Xia, G. Sun, J. Kim, et al., Multi-scale modeling and simulation of additive manufacturing based on fused deposition technique, Phys. Fluids 35 (3) (2023).
[16] J. Kim, A generalized continuous surface tension force formulation for phase-field models for multi-component immiscible fluid flows, Comput. Methods Appl. Mech. Engrg. 198 (37–40) (2009) 3105–3112.
[17] B. Jiang, Q. Xia, J. Kim, et al., Efficient second-order accurate scheme for fluid–surfactant systems on curved surfaces with unconditional energy stability, Commun. Nonlinear Sci. Numer. Simul. 135 (2024) 108054.
[18] X. Pan, S. Chun, J.I. Choi, Efficient monolithic projection-based method for chemotaxis-driven bioconvection problems, Comput. Math. Appl. 84 (2021) 166–184.
[19] X. Pan, K. Kim, C. Lee, et al., A decoupled monolithic projection method for natural convection problems, J. Comput. Phys. 314 (2016) 160–166.
[20] X. Xiao, Z. Dai, X. Feng, A positivity preserving characteristic finite element method for solving the transport and convection–diffusion–reaction equations on general surfaces, Comput. Phys. Comm. 247 (2020) 106941.
[21] W. Xie, Q. Xia, Q. Yu, et al., An effective phase field method for topology optimization without the curvature effects, Comput. Math. Appl. 146 (2023) 200–212.
[22] X. Xiao, K. Wang, X. Feng, A lifted local Galerkin method for solving the reaction–diffusion equations on implicit surfaces, Comput. Phys. Comm. 231 (2018) 107–113.
[23] Q. Xia, J. Kim, B. Xia, et al., An unconditionally energy stable method for binary incompressible heat conductive fluids based on the phase–field model, Comput. Math. Appl. 123 (2022) 26–39.
[24] Z. Tan, L. Chen, J. Yang, Generalized Allen–Cahn-type phase-field crystal model with FCC ordering structure and its conservative high-order accurate algorithm, Comput. Phys. Comm. 286 (2023) 108656.

[25] S. Zhai, Z. Weng, Y. Mo, et al., Energy dissipation and maximum bound principle preserving scheme for solving a nonlocal ternary Allen–Cahn model, Comput. Math. Appl. 155 (2024) 150–164.
[26] Z. Weng, S. Zhai, W. Dai, et al., Stability and error estimates of Strang splitting method for the nonlocal ternary conservative Allen–Cahn model, J. Comput. Appl. Math. 441 (2024) 115668.
[27] D. Wang, X.P. Wang, X. Xu, An improved threshold dynamics method for wetting dynamics, J. Comput. Phys. 392 (2019) 291–310.
[28] Y. Li, Q. Xia, S. Kang, et al., A practical algorithm for the design of multiple-sized porous scaffolds with triply periodic structures, Math. Comput. Simulation 220 (2024) 481–495.
[29] X. Song, B. Xia, Y. Li, An efficient data assimilation based unconditionally stable scheme for Cahn–Hilliard equation, Comput. Appl. Math. 43 (3) (2024) 121.
[30] X. Song, Q. Xia, J. Kim, et al., An unconditional energy stable data assimilation scheme for Navier–Stokes-Cahn-Hilliard equations with local discretized observed data, Comput. Math. Appl. 164 (2024) 21–33.
[31] J. Kim, D. Jeong, S.D. Yang, et al., A finite difference method for a conservative Allen–Cahn equation on non-flat surfaces, J. Comput. Phys. 334 (2017) 170–181.
[32] Y. Li, R. Liu, Q. Xia, et al., First-and second-order unconditionally stable direct discretization methods for multi-component Cahn–Hilliard system on surfaces, J. Comput. Appl. Math. 401 (2022) 113778.
[33] Q. Xia, Y. Liu, J. Kim, et al., Binary thermal fluids computation over arbitrary surfaces with second-order accuracy and unconditional energy stability based on phase-field model, J. Comput. Appl. Math. 433 (2023) 115319.
[34] J. Yang, Z. Tan, Simple and practical method for the simulations of two-component PFC models for binary colloidal crystals on curved surfaces, Int. J. Mech. Sci. 225 (2022) 107342.
[35] B. Xia, X. Xi, R. Yu, et al., Unconditional energy-stable method for the Swift–Hohenberg equation over arbitrarily curved surfaces with second-order accuracy, Appl. Numer. Math. 198 (2024) 192–201.
[36] J. Shen, J. Xu, J. Yang, The scalar auxiliary variable (SAV) approach for gradient flows, J. Comput. Phys. 353 (2018) 407–416.
[37] Y. Li, J. Yang, Consistency-enhanced SAV BDF2 time-marching method with relaxation for the incompressible Cahn–Hilliard–Navier–Stokes binary fluid model, Commun. Nonlinear Sci. Numer. Simul. 118 (2023) 107055.
[38] H.A. Van der Vorst, Bi-CGSTAB: A fast and smoothly converging variant of Bi-CG for the solution of nonsymmetric linear systems, SIAM J. Scient. Statist. Comput. 13 (2) (1992) 631–644.